STARS

Smart Material Actuation and Morphing for Unmanned Aircraft Systems

Caio H. Da Silva Lima
University of Central Florida

Part of the Aerospace Engineering Commons

Find similar works at: https://stars.library.ucf.edu/honorstheses

University of Central Florida Libraries http://library.ucf.edu

University of Central Florida

STARS
Showcase of Text, Archives, Research & Scholarship

SMART MATERIAL ACTUATION AND MORPHING FOR UNMANNED AIRCRAFT SYSTEMS

by

CAIO H. DA SILVA LIMA

A thesis submitted in partial fulfillment of the requirements
for the Honors in the Major Program in Aerospace Engineering
in the College of Engineering and Computer Science
and in the Burnett Honors College
at the University of Central Florida
Orlando, Florida

Summer Term, 2016

Thesis Chair: Jeffrey L. Kauffman, Ph.D.

ABSTRACT

The intent of this thesis is to outline the design, analysis, and characterization of an axially compressed piezocomposite actuator and, in particular, to determine the correlation and accuracy of two models used to predict deflection of an axially compressed piezocomposite bimorph. Restrictions in material properties lead to vehicle inefficiencies caused by the discontinuous geometry of deflected control surfaces in unmanned aircraft systems. This performance disadvantage in discrete control surfaces is caused in part by the sharp edges that are formed when the surface is pivoted. Flow continuity over the body of a vehicle is important in minimizing the effects of drag and, in turn, increasing aerodynamic performance. An efficient alternative to discrete control surface actuation is axially compressed piezocomposite actuation which could potentially improve the efficiency of the vehicle in all environments. Bimorph performance in angular deflection and displacement for the PA16N and MFC-M8528-P1 piezocomposites is analyzed using a Classical Laminate Plate Theory (CLPT) model and an Elastica model. Model accuracy is verified through experimental testing of a PA16N bimorph. CLPT model is shown to be accurate to within .05 mm and Elastica model is shown to be accurate to within .04 mm for axial forces below 30 N. Correlation between the mathematical models is confirmed. Experimental results for the PA16N show that a 30 N compression force applied to the bimorph can increase the maximum displacement by approximately 2.5 times the original displacement.

DEDICATION

To my mother and father who have supported me unconditionally and without whom I would not be able to be here.

ACKNOWLEDGEMENTS

TABLE OF CONTENTS

LIST OF FIGURES

LIST OF TABLES

LIST OF ABBREVIATIONS

IDE – Interdigitated Electrode

MFC – Macro Fiber Composite

PZT – Lead Zirconate Titanate

UAS – Unmanned Aircraft Systems

UAV – Unmanned Aerial Vehicle

UCAV - Unmanned Combat Aerial Vehicle

INTRODUCTION

Fixed wing aircraft design substitutes optimum efficiency for versatility such that the vehicle may fly in diverse conditions but at subprime performance. [1] Due to material restrictions, discontinuous geometry is the cost of actuation for control surfaces, which contributes to vehicle inefficiency in UAS. Discrete control surfaces owe their performance disadvantage to the sharp edges that are formed when the surface is pivoted. These sharp edges increase drag. [2] Continuity of flow over the body of a vehicle is essential in minimizing the effects of drag and, consequently, increasing aerodynamic performance. Contouring control surfaces are an alternative to discrete control surfaces that can potentially improve the efficiency of the vehicle in all environments.

Reliability issues also arise from the use of servos to drive hinged control surfaces. The intricacy of actuation systems and the number of parts involved in actuation increases the likelihood of failure. Williams [3] found that electromechanical failure was responsible for more UCAV accidents than human error. Logan et al. [4] noted that the combined in-use failure rate of both analog and digital servos in UAVs accounted for a quarter of component failures. Replacing servos with smart material actuators capable of conforming actuation could potentially reduce the number of parts in the vehicle, thereby increasing vehicle reliability. Solid state morphing, or shape changing, can be used to achieve conforming geometry of control surfaces. Smart materials have been previously employed in UAS as actuators to improve vehicle performance.

Smart materials, in general, take advantage of their inherent physical properties such that they convert a change in one property of the material to change in another

property of a material. Shape memory alloys, for example, take advantage of their crystal structures in different temperatures. When they are deformed from their original state and are then heated past a temperature that induces a transition in their crystal structure, they return to their original state. Piezoelectric materials take advantage of their crystal structure such that when the materials are under pressure of any kind and they deform from their original state, they generate a voltage. Piezoelectric materials also take advantage of the inverse of this process. When an electric field interacts with piezoelectric materials, they deform from their original state. This process has been exploited for the purpose of UAS actuation. Piezocomposite transducers consisting of piezoelectric material packaged with electrodes have had success when implemented in UAS for the purpose of actuation.

One piezocomposite transducer that is being considered for solid state actuation is the Macro Fiber Composite developed by NASA Langley Research Center. The MFC exploits high strain energy density, geometric compliance, durability, and high voltage-low power operation. [5] Despite improvements in piezoelectric actuation, the MFC still suffers from relatively low deflection, hysteresis, and anisotropic actuation. Another similar piezocomposite transducer under consideration is the Mide PA16N. Both transducers take advantage of interdigitated electrodes. IDEs allows for full coverage of the piezoelectric material, which is PZT. It also allows an electrode spacing that is less than 1 mm and it affords more flexibility to the piezocomposites.

However, control authority of a piezocomposite controlled aircraft has been an issue raised by many papers. Butt et al. [6] extensively documents flight control issues of an entirely smart material controlled aircraft. Ohanian et al. [7] reported low vehicle responsiveness and difficulty in managing the aircraft when control compensation algorithms were purposefully disabled mid-flight. With regards to piezoelectric actuated morphing vehicles, the two main control issues that arise are hysteresis and creep. Hysteresis is a systemic lag that stems from a non-linear response when compared to the input. Creep is a time-dependent deformation that inhibits the positional accuracy of the material although, hysteresis is the dominant non-linearity and its effects are immediately discernible. [8] Compensation for these non-linearities, most likely through a microcontroller platform, will be required for precise control of a solid state morphing aircraft.

One method of increasing the effectiveness of deformation in piezoelectric transducers involves configuring the elements in a bipolar bimorph configuration. [9] This layout involves fixing two piezoelectric transducers together such that the deflection of the elements is coupled. Post-buckled precompressed (PBP) actuation may also help to increase the deflection of piezoelectric transducers. PBP actuation increases the efficiency of energy conversion in the transducer by maintaining a compressive force on the piezoelectric actuator. [10]

Most commercially available IDE piezocomposite transducers operate predominantly by taking advantage of either the d_{31} or d_{33} piezoelectric strain coefficient. Of these PZT transducers, those that take advantage of the d_{33} piezoelectric strain

3

constant are typically more efficient at using an electric field to produce a mechanical response. This is attributed to the fact that the d_{33} piezoelectric strain coefficient is slightly more than double that of the d_{31}. [11] For instance, the MFC P1 type offered by Smart Material Corporation takes advantage of the d_{33} effect and could extend at most to 1800 $\mu\varepsilon$. The MFC P2 and P3 types, which utilize the d_{31} effect, could shrink up to 750 $\mu\varepsilon$.

Overall, the proposed research seeks to outline the design, analysis, and characterization of an axially compressed piezocomposite actuator that could potentially be implemented in a UAS to improve reliability and flight performance. The main intent of this thesis will be to directly compare the accuracy (through experimental verification) and correlation between two mathematical models used to predict the displacement and angular deflection of an axially compressed bimorph. Different numerical approaches from their original intention will be used to determine if a potential solution that models the deflection of an actuated and compressed bimorph may be found. Also, this thesis will be fielding a PA16N bipolar bimorph for actuation for the first time. The following sections will cover modeling analysis, experimental testing and the results of both for an axially compressed bimorph.

LITERATURE REVIEW

As advances in material science progress and with the commercial implementation of composites in aircraft, a surge of interest has been seen in morphing aircraft. This chapter provides a sample of the work that has led to development thus far in the area of smart material actuation and morphing aircraft.

Bolonkin and Gilyard [12] predicted potential aerodynamic performance benefits to transport aircraft for implementing variable camber control. The paper covered the factors that would influence the design of a variable-geometry wing. Specific calculations of the benefits of variable camber for the Lockheed L-1011 Tri-Star were presented for flight at Mach numbers at 0.6 and 0.83. The two main potential benefits of variable camber presented by the paper are the optimization of fuel consumption and speed. Wilkie et al. [5] divulged the development of the MFC. The paper outlines how the MFC is fabricated and what applications it is useful for. The MFC is made up of piezoceramic fibers sandwiched by IDEs affixed to polyimide film and held together by epoxy. The paper also characterizes the specific properties of the material. Gern et al. [13] showed that significant performance advantages could be attained by morphing wing structures as opposed to hinged control surfaces. The structural and aeroelastic response of a UCAV capable of camber and twist actuation was modeled and verified using MSC NASTRAN finite element analysis software. The paper outlines how higher roll moments were achieved by the morphing wing compared to a conventionally actuated wing. It was also determined that roll reversal occurred at higher dynamic pressures with the morphing wing than it did with the conventional wing.
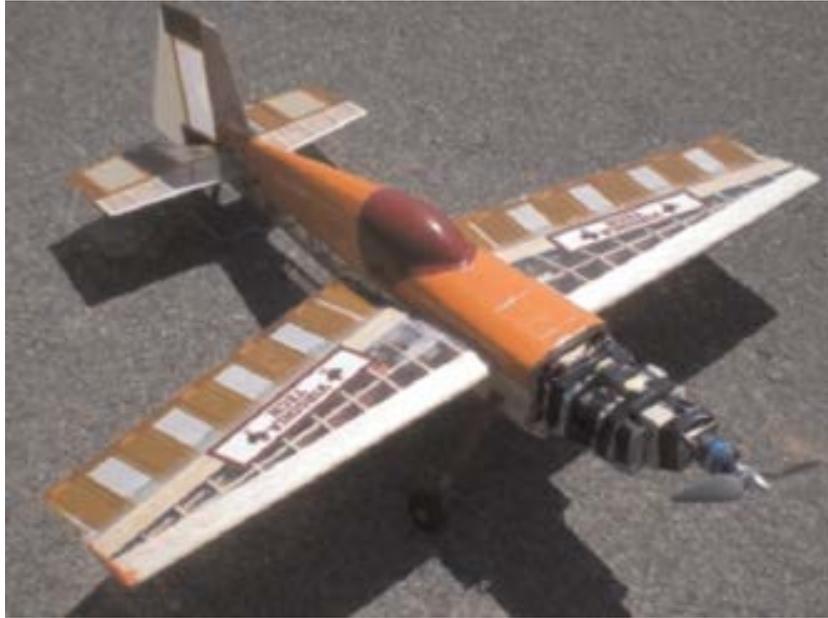
Figure 1 - Virginia Tech Morphing Aircraft [14]

Butt et al. [6] and Bilgen et al. [14] demonstrated that an aircraft solely controlled by MFC actuators was feasible. The papers present the "first fully solid-state piezoelectric material controlled, nontethered, flight tested fixed-wing aircraft" designed and flown by the 2010 Virginia Tech Wing Morphing Design Team. The team modified an Edge 540 remote controlled aircraft to employ a total of 36 individual MFC actuators in bimorph configuration for all control surfaces. The team also designed a circuit to accommodate high voltage DC-DC conversion and voltage asymmetry necessary for MFC actuation. It was noted that hysteresis and lag in control response compromised the stability of the aircraft in flight and led to several crashes. Notably, the morphing control surfaces survived all of these incidences, which the authors attribute to the ability of these surfaces to sufficiently dampen impact energy.

Barbarino et al. [1] summarized the advances of the state of the art in morphing aircraft design. The paper discusses the inspirations in nature for morphing aircraft and specific attempts to implement these characteristics in aircraft design. Specific morphing configurations and various implementations of these in different categories of vehicles are mentioned. The paper concludes by outlining advances needed for new methods of morphing to be successfully implemented in future aircraft.
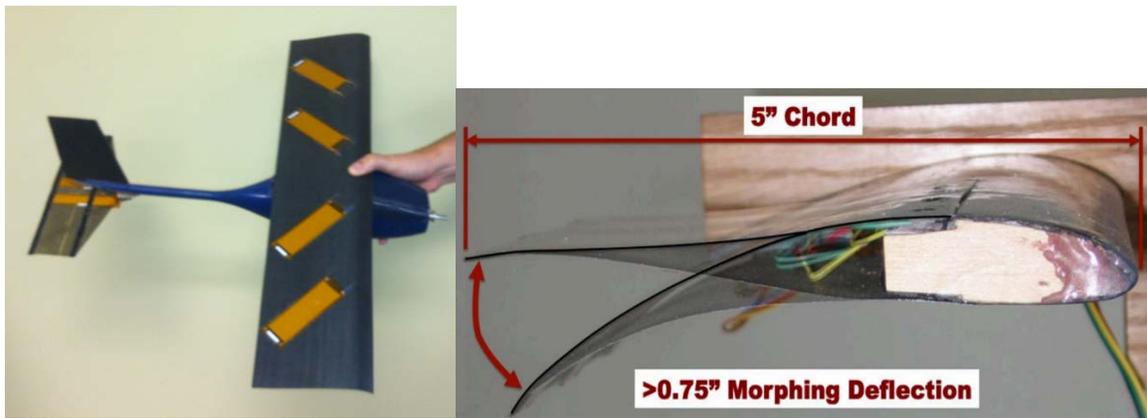
Figure 2 - Variable twist morphing wing on GENMAV vehicle [15] (left) and variable camber prototype [16] (right)

Ohanian et al. [7] [16] compared conventional servo-actuated control surfaces to similar MFC-actuated morphing control surfaces. The conventional setup consisted of hinged servo actuated ailerons and elevator. The morphing setup consisted of a morphing elevator and two different wing configurations. One wing was of variable camber design (Figure 2, right) and consisted of a thick airfoil cross section with a wiping lower surface that moved to accommodate the actuated upper surface. The other wing was of a variable twist design (Figure 2, left), which consisted of a thin airfoil cross section. Inverse hysteresis compensation was applied to the vehicle via the Ardupilot Mega

microcontroller platform. Probst et. al. [17] specifically describes the control law used and explores different methods of control augmentation that could be used to linearize actuation response for MFC actuated control surfaces. Specific advantages that were achieved by the morphing designs over conventional actuation include higher lift to drag ratio (and thus higher efficiency), low power consumption, 10 times actuation bandwidth of the servo, and longer life cycle of the MFC actuator.

In Smart Composites: Mechanics and Design, [18] Bilgen, Kochersberger and Inman summarize the basic design methodology of a MFC actuated morphing wing. The section specifically discusses the theoretical and experimental analysis of thin simply supported airfoil and thick cascading airfoil designs.
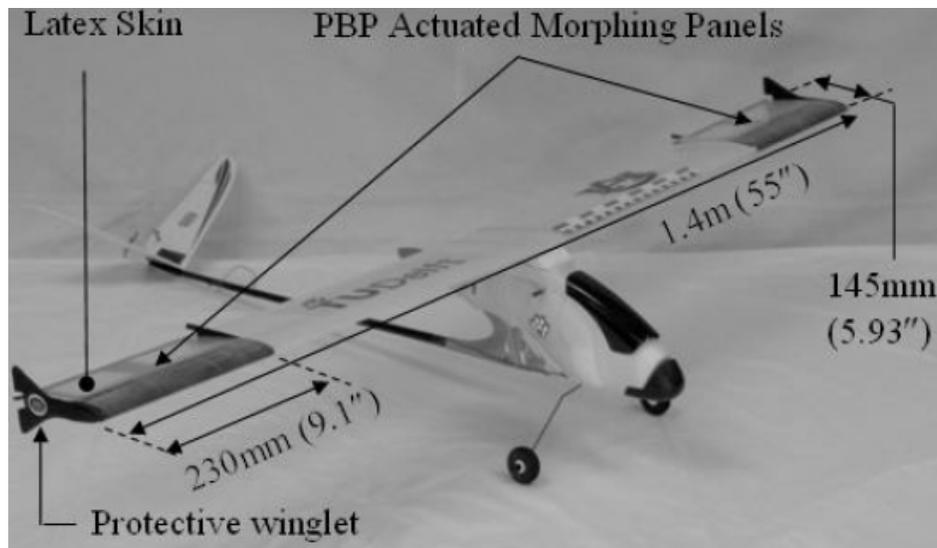
Figure 3 - PBP Actuated Morphing Vehicle [19]

Vos et al. [19] implemented Post-Buckled Precompressed piezoelectric actuation for a morphing wing. PBP actuation requires an axial precompression and a longitudinal

compressive force on the actuator. The axial precompression is imparted on the actuator by heating the bimorph during curing such that the mismatch in the coefficient of thermal expansion in the monolithic piezoelectric material and substrate compresses the bimorph. A CLPT model is used to characterize deflection for the PBP. Figure 3 shows the thick airfoil PBP actuated morphing wing on the test vehicle. The implementation of a compressive force to the piezoelectric actuated morphing wing more than doubled the deflection slope of the ailerons. By replacing servos with PBP actuators in the wing of a UAS, improvements in weight, actuator bandwidth, power consumption, and part count were achieved.

Wickramasinghe et. al. [20] proposed the implementation of a bimorph actuator with a compressive load by latex or an electroactive polymer skin for a smart wing on an extreme-agility MAV. An analytical model that was derived from the bending equilibrium equation, an aerodynamic model, and a FEM model was used to predict deflection for the smart wing. The models were experimentally verified with at most 24% variation for the analytical model and at most 8% variation for the FEM model.

ANALYSIS

CLPT MODEL

A deflection model for an axially compressed Piezocomposite bimorph actuator was adapted from a model constructed for Postbuckled Precompressed actuators by Vos et al. [21]. The model is designed to predict the symmetric deflection angle and displacement of a simply-supported bimorph actuator at a defined voltage with respect to the horizontal.

The model of the static deflection of the Axially Compressed bimorph actuator is derived from Classical Laminate Plate Theory. The planar forces and moments (N and M, respectively) of the actuator may be equated to the planar strain (ε) and curvature (κ) of the laminate by neglecting thermal and external stresses.

$$\begin{bmatrix} A & B \\ B & D \end{bmatrix} \begin{Bmatrix} \varepsilon \\ \kappa \end{Bmatrix} = \begin{bmatrix} A & B \\ B & D \end{bmatrix} \begin{Bmatrix} \Lambda \\ 0 \end{Bmatrix} \tag{1}$$

By assuming that the coupling stiffness (B) for the laminate is zero as a result of symmetry in both material property and geometry, the curvature of the laminate (sans applied force) can be determined by simplifying the second equation of the system for κ with respect to free strain of the actuator (Λ).

$$\kappa = \frac{B}{D}\Lambda \tag{2}$$

The simplified laminate-bending stiffness, in accordance with CLPT, is given by:

$$D = \frac{E_s t_s^{\,3}}{12} + \frac{2}{3}E_b\left(\left(\frac{t_s}{2}+t_b\right)^3 - \left(\frac{t_s}{2}\right)^3\right) + \frac{2}{3}\left(\left(\frac{t_s}{2}+t_b+t_a\right)^3 - \left(\frac{t_s}{2}+t_b\right)^3\right) \tag{3}$$

In the equation above, E represents the Young's Modulus and t represents the thickness of a component. With regards to the subscripts, s represents the substrate, b represents the bonding layer, and a represents the piezocomposite actuator.

The simplified coupling stiffness for the actuator relative to the laminate is:

$$B = E_a \left(\left(\frac{t_s}{2} + t_b + t_a \right)^2 - \left(\frac{t_s}{2} + t_b \right)^2 \right) \tag{4}$$

The free strain of the actuator may be determined by:

$$\Lambda = \frac{d_{3x}V}{t_{elec}} \tag{5}$$

For the equation above, d_{3x} represents the dominant piezoelectric strain constant, V represents the voltage supplied to the actuators, and t_{elec} represents the distance between the electrodes of the actuators.

Now considering an axial force (F), the product of the change in the angle (δ) of a section of the laminate with respect to the surface of the laminate (s) and the distance y above the x-axis is equivalent to the planar strain.

$$\varepsilon = y\frac{d\delta}{ds} \tag{6}$$

Using Hooke's Law and assuming the laminate experiences pure bending, the planar strain of the laminate due to pure bending is:

$$\varepsilon = \frac{My}{EI} \tag{7}$$

The moment due to the axial compression force is:

$$M = -Fy \tag{8}$$

In accordance with CLPT conventions,

$$\frac{d\delta}{ds} = -\frac{F}{Db}y \tag{9}$$

The relationship between y, s, and δ at a specific point in the laminate is given by:

$$\sin(\delta) = \frac{dy}{ds} \tag{10}$$

Such that when the previous equation is differentiated with respect to s:

$$\frac{d^2\delta}{ds^2} = -\frac{F \sin(\delta)}{Db} \tag{11}$$

In order to make the equation integrable, both sides are multiplied by an integrating factor of $\frac{d\delta}{ds}$ and then integrated and simplified to attain:

$$\left(\frac{d\delta}{ds}\right)^2 = \frac{2F \cos(\delta)}{Db} + C \tag{12}$$

where C is a constant of integration. At x=0, the laminate angle $\delta = \delta_0$. Assuming that $\frac{d\delta}{ds} = \kappa$ at x=0:

$$C = \kappa^2 - \frac{2F\cos(\delta_0)}{Db} \tag{13}$$

After substituting and simplifying:

$$\frac{d\delta}{ds} = -\sqrt{\frac{2F(\cos(\delta) - \cos(\delta_0))}{Db} + \kappa^2} \tag{14}$$

Note that the root is negative because $\frac{d\delta}{ds}$ is always negative as a result of the negative concavity. After applying double-angle trigonometric identities, the equation becomes:

$$\frac{d\delta}{ds} = -\sqrt{\frac{2F\left(1 - 2\sin^2\left(\frac{\delta}{2}\right) - 1 + 2\sin^2\left(\frac{\delta_0}{2}\right)\right)}{Db} + \kappa^2} \tag{15}$$

After simplification:

$$\frac{d\delta}{\sqrt{\left(\sin^2\left(\frac{\delta_0}{2}\right) - \sin^2\left(\frac{\delta}{2}\right)\right) + \frac{\kappa^2 Db}{4F}}} = -2\sqrt{\frac{F}{Db}}\,ds \tag{16}$$

At x=L/2, the angle of the laminate δ is equal to zero. Considering the symmetry of the beam, the problem may be simplified to allow both sides of the equation to be integrated such that:

$$\sqrt{\frac{F}{Db}}\int_0^{.5} ds = \frac{L}{2}\sqrt{\frac{F}{Db}} = \int_0^{\delta_0} \frac{d\delta}{2\sqrt{\left(\sin^2\left(\frac{\delta_0}{2}\right) - \sin^2\left(\frac{\delta}{2}\right)\right) + \frac{\kappa^2 Db}{4F}}} \tag{17}$$

The equation above may then be solved numerically to determine the tip to tip deflection of the actuator. However, the problem could also be solved as a boundary value problem using the bvp4c solver in MATLAB (as shown in Appendix A) and the initial and midpoint condition for curvature and angular deflection, respectively.

13

ELASTICA MODEL

An analytical model for a simply-supported axially compressed piezocomposite bimorph was adapted from a model for an axially compressed piezoelectric bimorph bender from Wickramasinghe et. al. [20]. The model is based off of Euler's Elastica equation which is derived from the relationship between moment and curvature. The model is modified to provide a more accurate high deflection analysis of the effects of axial compression on a simply supported piezocomposite bimorph.

The governing differential equation for this model is:

$$\frac{d^2y}{dx^2} = \left(\frac{Fy}{EI} + \frac{M}{EI}\right)\left(1 + \left(\frac{dy}{dx}\right)^2\right)^{1.5} \tag{18}$$

For the equation above, M represents the moment generated by the piezocomposite actuators and F represents the axial compression force on the bimorph.

The flexural rigidity for the bimorph is determined by the equation:

$$EI = b\left[\frac{E_s t_s{}^3}{12} + E_b t_b\left(\frac{t_b{}^2}{6} + \frac{(t_s + t_b)^2}{2}\right) + 2E_a t_a\left(\frac{t_a{}^2}{12} + \left(t_b + \frac{t_p + t_s}{2}\right)^2\right)\right] \tag{19}$$

Similarly to the previous model, E represents the Young's Modulus, t represents the thickness of a component, and b represents the width of the bimorph. The equation assumes that the width of all components of the bimorph are equal. For the subscripts, s represents the substrate, b represents the bonding layer, and a represents the piezocomposite actuator.

The moment generated by the piezocomposite actuators is defined by the equation:

$$M = -E_a b \frac{d_{31} V}{t_{elec}} (t_a^2 + t_s t_a + 2 t_b t_a) \tag{20}$$

From here, the model is solved numerically using the bvp4c solver in MATLAB as is shown in Appendix B. The simply supported set up is symmetric. As such, the solver is set up to solve one half of the bimorph only.

RESULTS

Table 1 - MFC M-8528-P1 and PA16N Properties

Item	MFC M-8528-P1	PA16N	Units
Width	0.028	0.030226	m
Length	0.085	0.05408	m
Actuator Thickness	0.0003	0.00033	m
Electrode Spacing	0.000508	0.00033	m
d33/d31	4.00E-10	1.79E-10	m/V
Elastic Modulus	3.03E+10	1.73E+10	Pa

The PA16N and the MFC-M8528-P1 were both analyzed using the CLPT and Elastica Models. The model assumed that a maximum of 1500 V and 200 V were applied to the MFC M-8528-P1 and PA16N, respectively. Table 1 shows the properties applied to the model. The model assumed an Aluminum substrate of 0.02743 mm and a bonding layer thickness of 0.0894 mm. In addition, the model varies the axial force from 0 N to 30 N in increments of 5.

Figure 4 - PA16N Deflection Angle at 200 V using CLPT and Elastica Models

Figure 4 shows the predicted angular deflection for a PA16N bimorph at a maximum voltage of 200 V using the CLPT and Elastica Models. Note that s represent the distance along the length of the bimorph.

Figure 5 - PA16N Displacement at 200 V using CLPT and Elastica Models

Figure 5 shows the predicted displacement for a PA16N bimorph with the same conditions as the previous figure. The theoretical displacement predicted for the PA16N is also relatively small for both models.
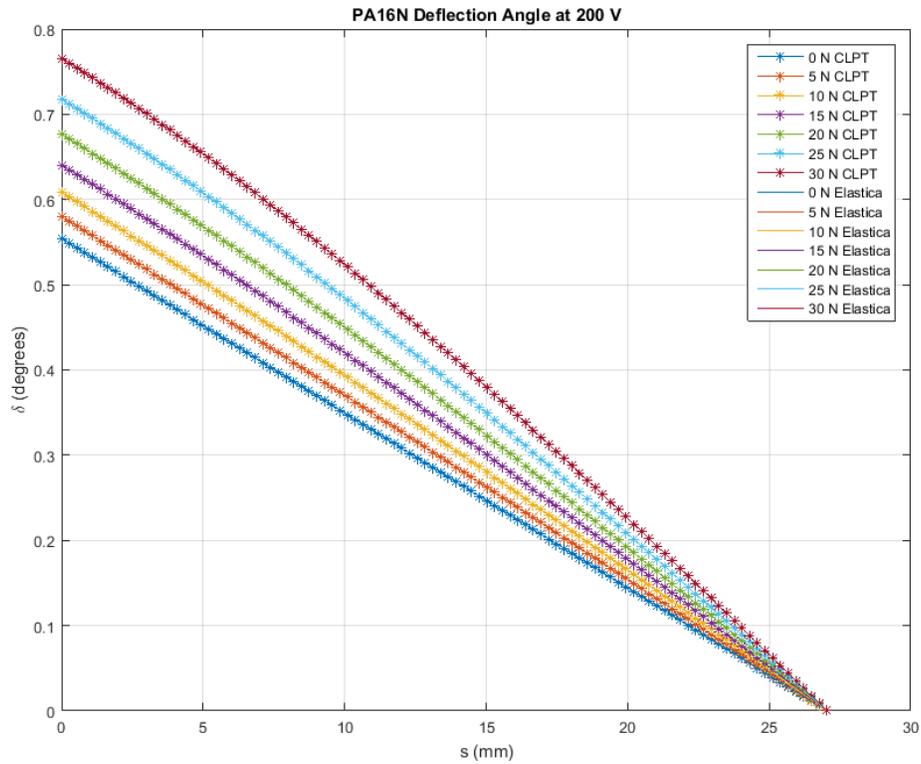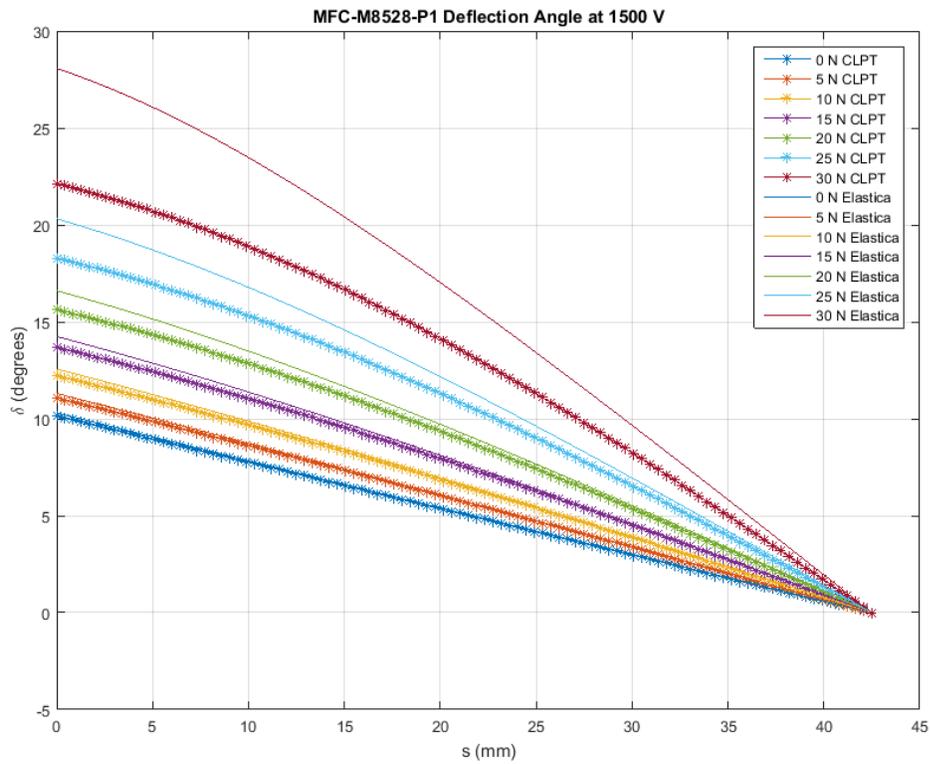
Figure 6 - MFC-M8528-P1 Deflection Angle at 1500 V using CLPT and Elastica Models

Figure 6 shows the predicted angular deflection for an MFC-M8528-P1 bimorph at a maximum voltage of 1500 V using the CLPT and Elastica models. The discrepancy between the two models is very close at lower axial forces but increases gradually.

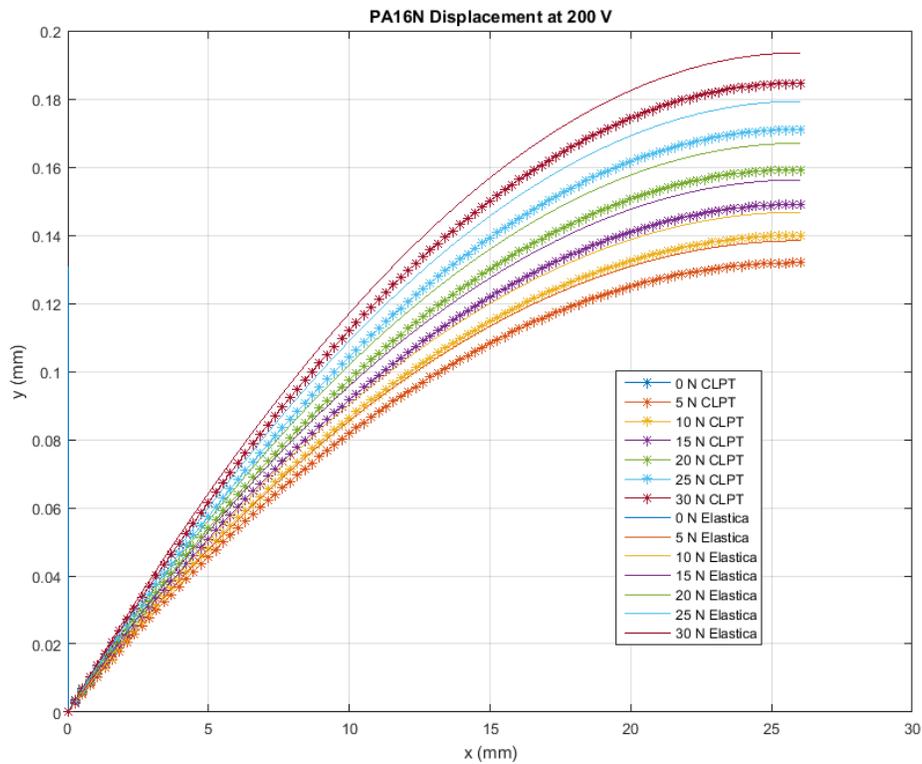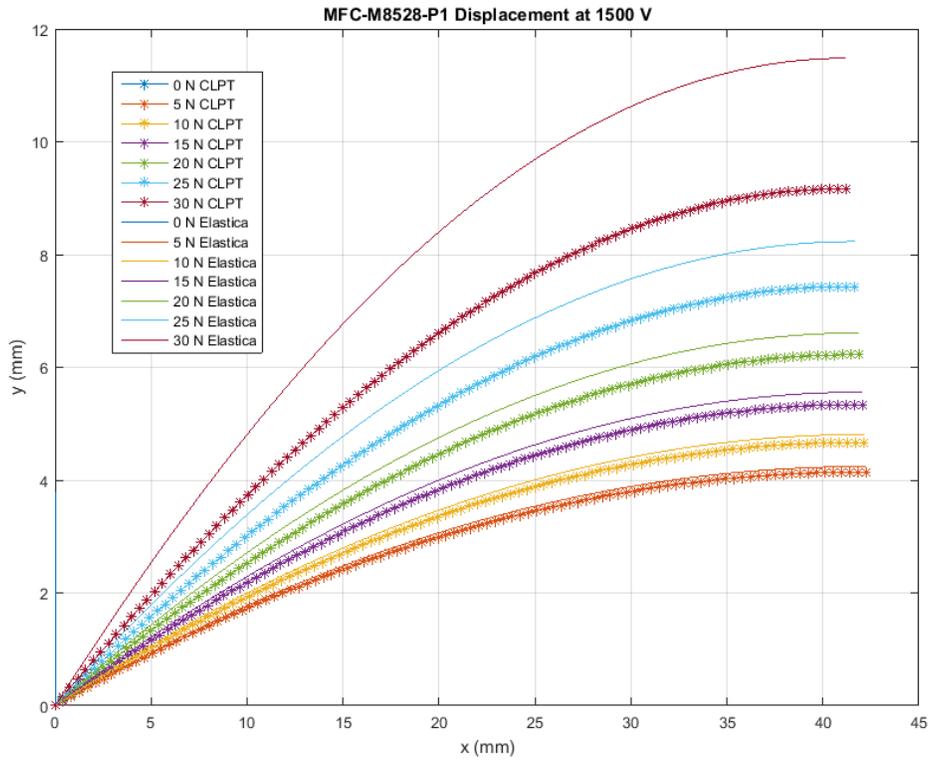Figure 7 - MFC-M8528-P1 Displacement at 1500 V using CLPT and Elastica Model

Figure 7 shows the predicted displacement for an MFC-M8528-P1 bimorph with the same conditions as the previous figure. The theoretical angular deflection and displacement for the MFC actuator is significantly greater than that of the PA16N. It also appears that the MFC bimorph is more sensitive to axial compression than the PA16N.

Table 2 – PA16N Theoretical Maximum Angular Deflection

Axial Force (N)	Max. Deflection (°)		% Difference
	PA16N CLPT	PA16N Elastica	
0	0.554	0.554	0.000
5	0.580	0.580	0.000
10	0.608	0.608	0.000
15	0.640	0.640	0.000
20	0.677	0.677	0.001
25	0.718	0.718	0.001
30	0.766	0.766	0.001

Table 2 shows the predicted maximum angular deflection for a given axial force for the PA16N using both models. It also lists the percent difference between the figures for the two models. From no axial compression to a 30 N axial force, both the CLPT and the Elastica models predicts a 38.3% increase in angular deflection for the PA16N.

Table 3 - PA16N Theoretical Maximum Displacement

Axial Force (N)	Max. Displacement (mm)		% Difference
	PA16N CLPT	PA16N Elastica	
0	0.125	0.131	4.803
5	0.132	0.138	4.792
10	0.140	0.147	4.781
15	0.149	0.156	4.770
20	0.159	0.167	4.759
25	0.171	0.179	4.749
30	0.185	0.194	4.738

Table 3 shows the maximum displacement predicted by the models for a given axial force for the PA16N. The percent difference between the figures for the two models

is also listed. From no axial compression to a 30 N axial force, the CLPT model predicts a 48% increase while the Elastica model predicts a 48.1% increase in maximum displacement for the PA16N.

Table 4 - MFC-M8528-P1 Theoretical Maximum Angular Deflection

| Axial Force (N) | Max. Deflection (˚) | | % Difference |
	MFC-M8528-P1 CLPT	MFC-M8528-P1 Elastica	
0	10.152	10.312	1.565
5	11.076	11.306	2.053
10	12.225	12.567	2.757
15	13.693	14.240	3.915
20	15.629	16.602	6.036
25	18.288	20.315	10.502
30	22.118	28.069	23.718

Table 4 displays the maximum angular deflection predicted by the two models for a given compression force on the MFC-M8528-P1. The table also lists the percent difference between the numbers for the two models. The CLPT model predicts an increase in maximum angular deflection of 2.17 times the no axial force deflection. The Elastica model predicts an increase of 2.72 times the no axial force deflection.

Table 5 - MFC-M8528-P1 Theoretical Maximum Displacement

Axial Force (N)	Max. Displacement (mm)		% Difference
	MFC-M8528-P1 CLPT	MFC-M8528-P1 Elastica	
0	3.717	3.795	2.058
5	4.140	4.242	2.446
10	4.666	4.811	3.055
15	5.338	5.561	4.093
20	6.222	6.610	6.037
25	7.433	8.231	10.198
30	9.161	11.482	22.484

Table 5 displays the maximum predicted displacement for the MFC-M8528-P1 using both models for the forces applied. The percent difference between the results of the two models are displayed in the table. The CLPT and Elastica models predict an increase in maximum displacement of 2.46 and 3.03 times the no axial load value, respectively.

The percent difference between the two models for the PA16N was very small, particularly with the predictions for angular deflection. The difference between the models for the MFC-M8528-P1 were slightly greater with higher axial force predictions. This could perhaps be due to issues with numerical resolution in the MFC Elastica model since the model experienced issues converging above 30 N. However, to prevent potential damage to the bimorphs, experimental testing will only be performed up to 30 N. The overall deflection for the MFC bimorph is greater than that of the PA16N bimorph. This is due to a combination of multiple factors with the predominant factors being the greater bimorph length and higher dominant piezoelectric strain constant.

EXPERIMENT

SET UP

In order to investigate the accuracy of the models in predicting actuation, a test bed was designed such that varying degrees of axial compression could be applied to an actuator. The test bed will also assist in evaluating the efficacy of axial compression of a piezocomposite bimorph. In order to allow for consistent measurements of the axial force on the actuator and to maintain design simplicity, a two section, simply supported set up was selected to investigate model accuracy and compression efficiency.
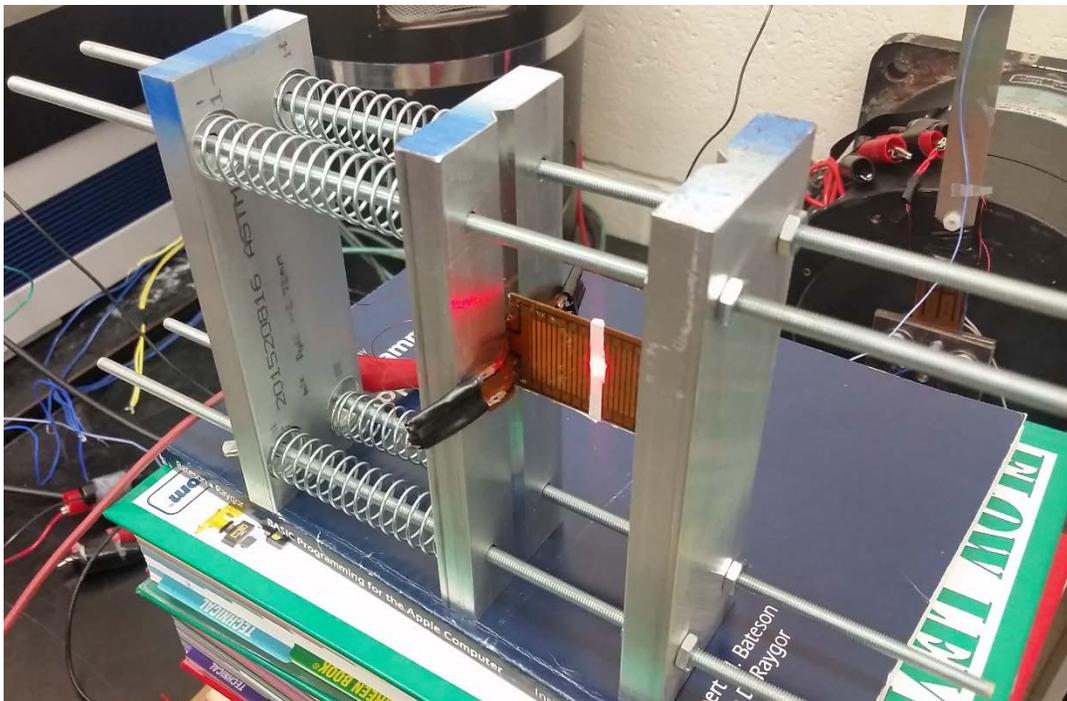

Figure 8 - Axial Compression Test Rig with PA16N Bimorph

The test rig, shown in Figure 8, is split into the spring section and the actuator housing section. The spring section consists of 4 compressions springs each with a spring constant rated at 1.9 lbs./inch. They are held in place by holes grooved into the aluminum

plates that sandwich them. The actuator housing section has aluminum plates that are v-notched to allow the actuator to deflect while remaining firmly in place. This set up allows for the axial compression force to be tailored by bringing the plates closer together using wing nuts on the opposite end of the rig. The force on the actuator may be determined by measuring the displacement of the springs.

As a result of availability, the Mide PA16N will be used in the experiment. The PA16N is a piezocomposite transducer which consists of thin strips of piezoelectric PZT sandwiched by IDEs and an outer layer of Kapton tape. The dominant piezoelectric effect governing this transducer is the d31 effect. As was previously discussed, the d31 effect is not as efficient as the d33 effect for electrical to mechanical coupling for transducers of this nature. As a result, the deflection of the bimorph will be small but sufficient for establishing the accuracy of the models.

Figure 9 - Trek Model 2205 High Voltage Amplifier

The PA16N was powered by the Trek Model 2205 High Voltage Amplifier. The amplifier, shown in Figure 9, is capable of supplying the ±200 V needed for the experiment. Measurements were collected using the Polytec OFV-5000 and the OFV-505. Data acquisition was performed using the National Instruments NI 9234 DAQ and LabView software.

RESULTS

For each axial force, 5 trials measuring the maximum displacement of the bimorph were performed. The first was a 40 second recording of a 0 V reading. The second and third trials consisted of manual square wave inputs sweeping in sequence from 0 V, 200 V, 0 V, -200 V, 0 V, 200 V, to 0 V. For the fourth and final trials, manual square wave

sequences from 0 V, -200 V, 0 V, 200 V, 0 V, -200 V, to 0 V, consecutively, were applied. Time increments between all inputs lasted approximately 5 seconds.

Table 6 - PA16N Test Results

Force (N)	Mean Displacement (mm)	Confidence Interval (99%)
0	0.081	0.008
5	0.101	0.012
10	0.123	0.011
15	0.157	0.014
20	0.174	0.018
25	0.175	0.018
30	0.203	0.021

Table 6 shows results for all trials collected for the PA16N bimorph at the specified compressive force. Some effects were noticeable from the experiments. Creep in actuation was very noticeable in the data, which is a characteristic of piezoelectric materials when used for actuation. The bimorph also experienced asymmetric deflection which could perhaps be due to its natural curvature or to manufacturing issues. Hysteresis in actuation was also very noticeable from the data gathered, which is also typical of piezoelectric materials used in actuation.
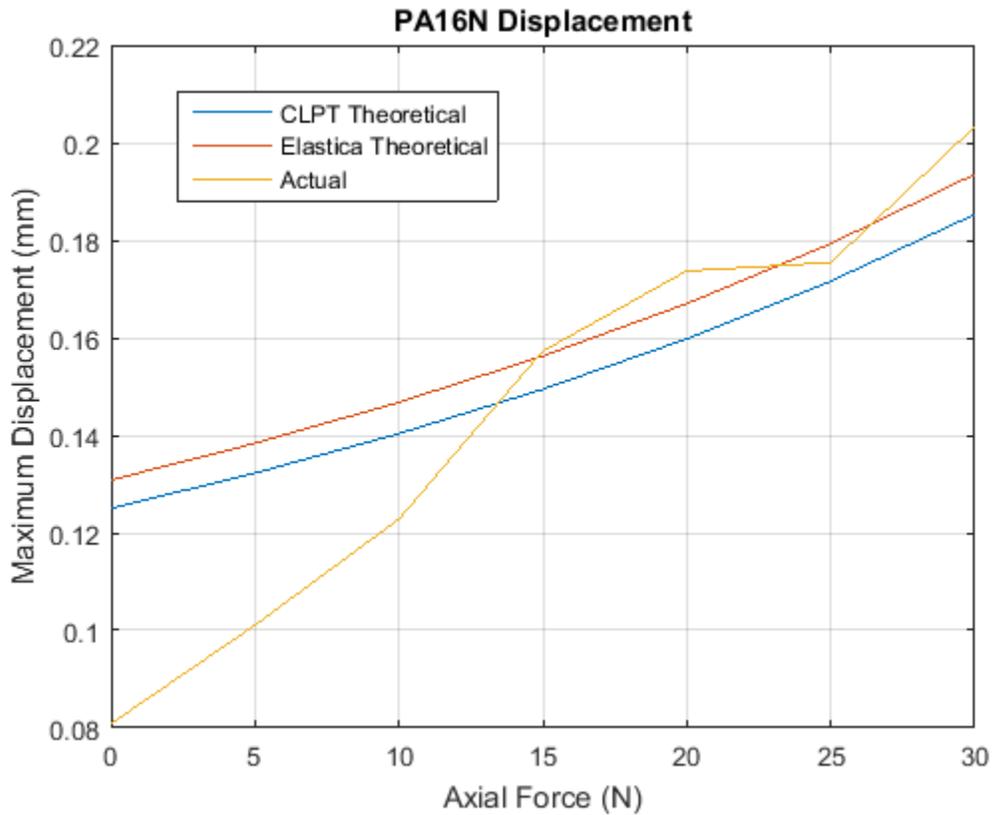
Figure 10 - PA16N Maximum Displacement Data Comparison

Figure 10 shows a plot comparing the theoretical and experimental maximum displacements for a given axial force on the PA16N bimorph. The largest discrepancy between the experimental results and the theoretical predictions was at the 0 N readings. The discrepancy found in the experimental maximum deflection value at low axial forces could be attributed to the insufficient support of the v-notch design of the test bed on the bimorph. However, the difference between the CLPT model and the experimental results for a 0 N axial force was .044 mm and the difference between the Elastica model and the experimental results for a 0 N axial force was .05 mm. An error of .05 mm is still a close correlation. As the axial force approaches 15 N, the measured maximum displacement

appears to follow closer to the model as the v-notch lends more support to the actuator

to deflect properly.

CONCLUSION

In order to determine whether an axially compressed piezocomposite bimorph could provide sufficient actuation for implementation in UAS, two models were invoked to characterize actuation behavior. The accuracy of these models were then experimentally verified to determine whether the piezocomposite bimorphs could be used for actuation and how significant an axial force on an IDE piezocomposite bimorph could contribute to a change in deflection characteristics.

All in all, correlation between the CLPT and Elastica models was substantiated by the calculations performed. The relatively small size and low deflection, despite axial compression, of the PA16N bimorph preclude their implementation in UAS. However, the PA16N has shown that the mathematical models were sufficiently competent in predicting displacement with the CLPT model deviating at most .05 mm and the Elastica model deviating at most .04 mm from the experimental results. As such, with the proven efficacy of the models, the MFC-M8528-P1 may be a good candidate for implementation in UAS given its relatively large predicted deflections. The PA16N experimental results also show that despite the low overall magnitude of deflection, applying a 30 N axial force to the bimorph, which originally has no axial force, can increase the maximum displacement by 2.5 times the original displacement.

Further testing could be performed to characterize the behavior of axially compressed P1-type MFC bimorphs in their different configurations, with different substrates, and with different actuation set ups. This same testing could also be performed on an axially-compressed IDEAL actuator (which, in essence, is an IDE and

PZT stack transducer), which has been shown to produce improved efficiency in actuation from MFCs. [11] In the experiments performed, open-loop control of the bimorph was used. As such, hysteresis in actuation was evident in the data. Before implementation in a UAS, hysteresis compensation through closed-loop control of the actuator must also be implemented. This could potentially include a method by which real-time tip position of the smart material actuated control surface is fed to a microcontroller such that the position required by the pilot is established to be that of the actuated surface.

APPENDIX A
CLPT MATLAB CODE

```matlab
%clptBVPPA16Nfin.m
clear
clc
Ea=1.7255e10; % measured
Es=70e9;
Eb=3.378e9
ta=0.0003302;
ts=2.743e-5; % measured
tb=8.94e-5; % measured
tel=ta; %electrode spacing in meters
l=.05408;
b=.030226; %PA16N
Vm=[200];
Fax=[0,5,10,15,20,25,30]; %N
B=(Ea*[ts*ta+2*tb*ta+ta*ta]);
D=(([Es*ts^(3)]/12)+Ea*[([ta*(ts+2*tb)^(2)]/2)+(ta*ta*(ts+2*tb))+(2*ta^(3)/3)
])+Eb*((2/3)*tb^(3)+tb^(2)*ts+.5*tb*ts^(2)));

d31=179e-12;
Lambda=(d31*Vm)/(tel);
kappa=(B/D)*Lambda;

for i=1:size(Fax,2)
    F=Fax(1,i);
    ini=bvpinit(linspace(0,l/2,10), [0,0]);
    sol=bvp4c(@CLPTrhs,@CLPTbc,ini);
    x=linspace(0,l/2,100);
    delta=deval(sol,x)*(180/pi);
    del(i,:)=transpose(delta(1,:));
    kap(i,:)=delta(2,:);
end
plot(x*1000,del), xlabel('s (mm)'), ylabel('\delta (degrees)'), title('PA16N
Deflection Angle at 200 V')
grid on
legend('0 N','5 N','10 N','15 N','20 N','25 N','30 N')

s=repmat(x,size(del,1),1);
v=zeros(size(s,1),size(s,2));
xi=zeros(size(s,1),size(s,2));

for i=2:size(s,1)
    for j=2:size(s,2)
        v(i,j)=v(i,j-1)+2.629797979797980e-04*sind(del(i,j))*1000; %mm
        xi(i,j)=xi(i,j-1)+2.629797979797980e-04*cosd(del(i,j))*1000; %mm
    end
end

figure
plot(xi',v'), xlabel('x (mm)'), ylabel('y (mm)'), title('PA16N Displacement
at 200 V')
grid on
legend('0 N','5 N','10 N','15 N','20 N','25 N','30 N')
```

```matlab
%CLPTrhs.m
function rhs=CLPTrhs(x,y)
F=evalin('base','F');
D=evalin('base','D');
b=evalin('base','b');

rhs=[y(2); -(F/(D*b))*sin(y(1))];
end



%CLPTbc.m
function bc=CLPTbc(yl,yr)
kappa=evalin('base','kappa');

bc=[yl(2)-kappa; yr(1)]



%clptBVPMFCM8528P1.m
clear
clc
b=28/1000 %m (width of actuator)
l=85/1000 %m (length of actuator)
tb=8.94e-5%m assumed bonding layer thickness
ta=.0003 %m (MFC thickness)
ts=2.743e-5 %m thickness of substrate (.02743 mm)
tel=0.000508 %m electrode spacing (d33)
d31=4e-10 % m/V (Actually d33)
Vm=[1500]; % Max Voltage
Ea=30.336e9 % Pa Actuator Young's Modulus
Eb=3.378e9 %Pa bonding layer Young's modulus
Es=70e9 %Pa Young's modulus of substrate (Aluminum)
Fax=[0,5,10,15,20,25,30]; %N
B=(Ea*[ts*ta+2*tb*ta+ta*ta]);
D=(([Es*ts^(3)]/12)+Ea*[(([ta*(ts+2*tb)^(2)])/2)+(ta*ta*(ts+2*tb))+(2*ta^(3)/3)
])+Eb*((2/3)*tb^(3)+tb^(2)*ts+.5*tb*ts^(2));
Lambda=(d31*Vm)/(tel);
kappa=(B/D)*Lambda;

for i=1:size(Fax,2)
    F=Fax(1,i);
    ini=bvpinit(linspace(0,l/2,10), [0,0]);
    sol=bvp4c(@CLPTrhs,@CLPTbc,ini);
    x=linspace(0,l/2,100);
    delta=deval(sol,x)*(180/pi);
    del(i,:)=transpose(delta(1,:));
    kap(i,:)=delta(2,:);
end
plot(x*1000,del), xlabel('s (mm)'), ylabel('\delta (degrees)'), title('MFC-
M8528-P1 Deflection Angle at 1500 V')
grid on
legend('0 N','5 N','10 N','15 N','20 N','25 N','30 N')
```

```
s=repmat(x,size(del,1),1);
v=zeros(size(s,1),size(s,2));
xi=zeros(size(s,1),size(s,2));

for i=2:size(s,1)
    for j=2:size(s,2)
        v(i,j)=v(i,j-1)+4.292929292929294e-04*sind(del(i,j))*1000; %mm
        xi(i,j)=xi(i,j-1)+4.292929292929294e-04*cosd(del(i,j))*1000; %mm
    end
end

figure
plot(xi',v'), xlabel('x (mm)'), ylabel('y (mm)'), title('MFC-M8528-P1
Displacement at 1500 V')
grid on
legend('0 N','5 N','10 N','15 N','20 N','25 N','30 N')
```

APPENDIX B
ELASTICA MATLAB CODE

```matlab
clear
clc
% PA16NElasticaBVPfin.m
b=.030226 %m (width of actuator)
l=.05408 %m (length of actuator)
tb=8.94e-5%m bonding layer thickness
ta=0.0003302 %m (PA16N thickness)
ts=2.743e-5 %m thickness of substrate (.02743 mm)
telec=ta %m electrode spacing (d31 top electrode to bottom electrode)
d31=179e-12 %m/V
V3=[200];
Ea=1.7255e10 %Pa
Eb=3.378e9 %Pa Bonding Layer Young's modulus
Es=70e9 %Pa Young's modulus of substrate
EI=2.*Eb.*b.*tb.*((tb.^(2)./12)+(.5.*ts+.5.*tb).^(2))+2.*Ea.*b.*ta*((ta.^(2).
/12)+(.5.*ts+.5.*ta+tb).^(2))+Es.*b.*ts.*(ts.^(2)./12)
M=-Ea*b*d31*(V3./telec)*(ta*ta+ts.*ta+2*tb*ta)
Fax=-[0,5,10,15,20,25,30]; % N

for i=1:size(Fax,2)
    F=Fax(1,i);
    ini=bvpinit(linspace(0,l/2,10), [0,0]);
    sol=bvp4c(@elastica,@ElasticaBVPbc,ini);
    x=linspace(0,l/2,100)
    v=deval(sol,x)
    deflection(i,:)=v(1,:)./.0254 % m to inches
    angle(i,:)=v(2,:)*(180/pi)%rads to degrees
end

xin=x.*39.3701;
xmm=x.*1000;
plot(xin,deflection), xlabel('x (in)'), ylabel('y (in)'), title('PA16N
Displacement at 200 V'), grid on
legend('0 N','5 N','10 N','15 N','20 N','25 N','30 N')
figure
plot(xmm,angle), title('PA16N Deflection Angle at 200 V'), xlabel('s (mm)'),
ylabel('\delta (degrees)'), grid on
legend('0 N','5 N','10 N','15 N','20 N','25 N','30 N')
figure
defmm=deflection.*.0254.*1000;
plot(xmm,deflection.*.0254.*1000), xlabel('x (mm)'), ylabel('y (mm)'),
title('PA16N Displacement at 200 V'), grid on
legend('0 N','5 N','10 N','15 N','20 N','25 N','30 N')


% elastica.m
function output=elastica(x,z)
M=evalin('base','M');
EI=evalin('base','EI');
F=evalin('base','F');
output=[z(2);((M/EI)+(F/EI)*z(1))*(1+(z(2))^(2))^(1.5)]
```

36

```matlab
%ElasticaBVPbc.m
function bc=ElasticaBVPbc(yl,yr)
bc=[yl(1); yr(2)]
end


clear
clc
% MFCM8528P1Elastica.m
b=28/1000; %m (width of actuator)
l=85/1000; %m (length of actuator)
tb=8.94e-5; % m assumed bonding layer thickness
ta=.0003; %m (MFC thickness)
ts=2.743e-5; %m thickness of substrate (.02743 mm)
tel=0.000508; %m electrode spacing (d31 top electrode to bottom electrode)
d31=4e-10; % m/V (d33)
Vm=[1500]; % Max Voltage
Ea=30.336e9; %Pa Actuator Young's Modulus
Eb=3.378e9; %Pa bonding layer Young's modulus
Es=70e9; %Pa Young's modulus of substrate
EI=2.*Eb.*b.*tb.*((tb.^(2)./12)+(.5.*ts+.5.*tb).^(2))+2.*Ea.*b.*ta*((ta.^(2).
/12)+(.5.*ts+.5.*ta+tb).^(2))+Es.*b.*ts.*(ts.^(2)./12);
M=-Ea*b*d31*(Vm./tel)*(ta*ta+ts.*ta+2*tb*ta); % Moment Due to Actuation
Fax=-[0,5,10,15,20,25,30]; %N Axial Compression

for i=1:size(Fax,2);
    F=Fax(1,i);
    ini=bvpinit(linspace(0,l/2,10), [0,0]);
    sol=bvp4c(@elastica,@ElasticaBVPbc,ini);
    x=linspace(0,l/2,100);
    v=deval(sol,x);
    deflection(i,:)=v(1,:)./.0254; % m to inches
    angle(i,:)=v(2,:)*(180/pi); % rads to degrees
end

xin=x.*39.3701;
xmm=x.*1000;
plot(xin,deflection), xlabel('x (in)'), ylabel('y (in)'), title('MFC-M8528-P1
Displacement at 1500 V'), grid on
legend('0 N','5 N','10 N','15 N','20 N','25 N','30 N')
figure
plot(xmm,angle), title('MFC-M8528-P1 Deflection Angle at 1500 V'), xlabel('s
(mm)'), ylabel('\delta (degrees)'), grid on
legend('0 N','5 N','10 N','15 N','20 N','25 N','30 N')
figure
defmm=deflection.*.0254.*1000;
plot(xmm,deflection.*.0254.*1000), xlabel('x (mm)'), ylabel('y (mm)'),
title('MFC-M8528-P1 Displacement at 1500 V'), grid on
legend('0 N','5 N','10 N','15 N','20 N','25 N','30 N')
```

REFERENCES

[1] S. Barbarino, O. Bilgen, R. M. Ajaj , M. I. Friswell and D. J. Inman, "A Review of Morphing Aircraft," *Journal of Intelligent Material Systems and Structures,* vol. 22, no. 9, pp. 823-877, June 2011.

[2] A. K. Jha and J. N. Kudva, "Morphing aircraft concepts, classifications, and challenges," in *Proceedings of Smart Structures and Materials 2004*, San Diego, CA, 2004.

[3] K. W. Williams, "A Summary of Unmanned Aircraft Accident/Incident Data: Human Factors Implications," FEDERAL AVIATION ADMINISTRATION OKLAHOMA CITY OK CIVIL AEROMEDICAL INST, Oklahoma City, OK, 2004.

[4] M. Logan, T. Vranas, M. Motter, Q. Shams and D. Pollock, "Technology challenges in small UAV development," in *Proceedings of InfoTech@Aerospace*, Arlington, VA, 2005.

[5] W. K. Wilkie, R. G. Bryant, J. W. High, R. L. Fox, R. F. Hellbaum, A. Jalink Jr, B. D. Little and P. H. Mirick, "Low-cost piezocomposite actuator for structural control applications," in *Proceedings of Symposium on Smart Structures and Materials*, Newport Beach, CA, 2000.

[6] L. Butt, S. Day, J. Weaver, C. Sossi, A. Wolek, O. Bilgen, W. Mason and D. Inman, "Wing morphing design utilizing macro fiber composite," in *Proceedings of Society of Allied Weight Engineers Annual Conference*, Virginia Beach, VA, 2010.

[7] O. Ohanian, B. David, S. Taylor, K. Kochersberger, T. Probst, P. Gelhausen and J. Climer, "Piezoelectric Morphing versus Servo-Actuated MAV Control Surfaces, Part II: Flight Testing," in *Proceedings of the Aerospace Sciences Meetings*, Grapevine, TX, 2013.

[8] X. Zhao, C. Zhang, H. Liu, G. Zhang and K. Li, "Analysis of hysteresis-free creep of the stack piezoelectric actuator," *Mathematical Problems in Engineering,* vol. 2013, no. 187262, May 2013.

[9] O. Bilgen, K. B. Kochersberger, D. J. Inman and O. J. Ohanian III, "Lightweight High Voltage Electronic Circuits for Piezoelectric Composite Actuators," *Journal of Intelligent Material Systems and Structures,* vol. 21, no. 14, pp. 1417-1426, September 2010.

[10] G. A. Lesieutre and C. L. Davis, "Can a Coupling Coefficient of a Piezoelectric Device be Higher Than Those of Its Active Material?," *Journal of Intelligent Material Systems and Structures,* vol. 8, no. 10, pp. 859-867, October 1997.

[11] K. J. Yoon, J. Lee, K. Kim, H. C. Park and N. S. Goo, "Design and Manufacturing of IDEAL with Stacked Ceramic Layers and Inter-Digitated Electrodes," *Key Engineering Materials,* Vols. 306-308, pp. 1175-1180, March 2006.

[12] A. Bolonkin and G. B. Gilyard, "Estimated Benefits of Variable-Geometry Wing Camber Control for Transport Aircraft," NASA Dryden Flight Research Center, Edwards Air Force Base, California, 1999.

[13] F. H. Gern, D. J. Inman and R. K. Kapania, "Structural and Aeroelastic Modeling of General Planform Wings with Morphing Airfoils," *AIAA Journal,* vol. 40, no. 4, pp. 628-637, April 2002.

[14] O. Bilgen, L. M. Butt, S. R. Day, G. A. Sossi, J. P. Weaver, A. Wolek, W. H. Mason and D. J. Inman, "A novel unmanned aircraft with solid-state control surfaces: Analysis and flight demonstration," *Journal of Intelligent Material Systems and Structures,* vol. 24, no. 2, pp. 147-167, January 2013.

[15] T. Probst, B. David, K. Kochersberger and O. Ohanian, "Design and Flight Test of Morphing UAV Flight Control System," in *Proceedings of the Aerospace Sciences Meeting*, Grapevine, TX, 2013.

[16] O. Ohanian, C. Hickling, B. Stiltner, E. Karni, K. Kochersberger, T. Probst, P. Gelhausen and A. Blain, "Piezoelectric Morphing versus Servo-Actuated MAV

Control Surfaces," in *Proceedings of AIAA/ASME/ASCE/AHS/ASC Structures, Structural Dynamics and Materials Conference*, Honolulu, HI, 2012.

[17] T. Probst, K. Kochersberger, B. Stiltner, C. Hickling, O. Ohanian, E. Karni, C. Olien and A. Blain, "Smart material actuators as a means of UAV flight control," in *Proceedings of Aerospace Sciences Meeting*, Nashville, TN, 2012.

[18] O. Bilgen, K. B. Kochersberger and D. J. Inman, "Wing Morphing Design Using Macro-Fiber Composites," in *Smart Composites: Mechanics and Design*, 2013, p. 169.

[19] R. Vos, R. Barrett, L. Krakers and M. van Tooren, "Post-buckled precompressed (PBP) piezoelectric actuators for UAV flight control," in *Proceedings of Smart Structures and Materials*, San Diego, CA, 2006.

[20] V. Wickramasinghe, C. Yong, M. Martinez, F. Wong and R. Kernaghan, "Design and verification of a smart wing for an extreme-agility micro-air-vehicle," *Smart Materials and Structures,* vol. 20, no. 12, 2011.

[21] R. Vos, R. Barrett, L. Krakers and M. van Tooren, "Post-buckled precompressed (PBP) piezoelectric actuators for UAV flight control," in *Proceedings of Smart Structures and Materials*, San Diego, CA, 2006.